OPEN ACCESS
IOP Publishing | Bureau International des Poids et Mesures Metrologia
Metrologia **62** (2025) 045008 (17pp) https://doi.org/10.1088/1681-7575/adf64a

Evaluation of a caesium fountain frequency standard for antihydrogen spectroscopy

J Nauta[1,2], E Thorpe-Woods[1], J Whale[4], A Wilson[4], A N Oliveira[3], V R Marshall[3], J Schoonwater[1], A Ashkhasi[4], C Ø Rasmussen[2], N Madsen[1], J S Hangst[3], K Gibble[5], K Szymaniec[4], R J Hendricks[4] and S Eriksson[1,*]

[1] Department of Physics, Faculty of Science and Engineering, Swansea University, Singleton Park, Swansea SA2 8PP, United Kingdom
[2] Experimental Physics Department, CERN, CH-1211 Genève 23, Switzerland
[3] Department of Physics and Astronomy, Aarhus University, DK-8000 Aarhus C, Denmark
[4] National Physical Laboratory, Teddington TW11 0LW, United Kingdom
[5] Department of Physics, The Pennsylvania State University, University Park, PA 16802, United States of America

E-mail: s.j.eriksson@swansea.ac.uk

Received 22 May 2025, revised 23 July 2025
Accepted for publication 31 July 2025
Published 22 August 2025

Abstract

The performance of a caesium fountain frequency reference for use in precision measurements of trapped antihydrogen in the ALPHA experiment at CERN is evaluated. A description of the fountain is provided together with a characterisation of systematic effects. The impact of the magnetic environment in the Antimatter Factory, where the fountain is installed, on the performance of the fountain is considered and shown to be insignificant. The systematic fractional frequency uncertainty of the fountain is 3.0×10^{-16}. The short-term frequency stability of the measured frequency from the ALPHA-HM1 maser is $1.5 \times 10^{-13}\tau^{-1/2}$, whereas the fountain itself shows a stability limit of $4.7 \times 10^{-14}\tau^{-1/2}$. We find a fractional frequency difference of $(1.0 \pm 2.2\ (\text{stat.}) \pm 6.5\ (\text{syst.})) \times 10^{-16}$ in a comparison with Terrestrial Time via a GNSS Common View satellite link between January 2023 and June 2024. The fountain enables a significant increase in frequency precision in antihydrogen spectroscopic measurements, and paves the way for improved limits on matter–antimatter comparisons.

Keywords: caesium fountain, antihydrogen, precision measurements, primary frequency standard, atomic clocks

* Author to whom any correspondence should be addressed.

1. Introduction

Charge-conjugation, parity-inversion, and time-reversal (CPT) invariance implies that bound states of antimatter exhibit an energy spectrum identical with their matter counterparts. To directly test CPT invariance, the ALPHA collaboration at CERN routinely measures frequencies corresponding to transitions between bound state energies of magnetically trapped antihydrogen [1–5]. The most precise measurement to date is on the 1S–2S transition frequency [6], which has been determined with a relative uncertainty of 2×10^{-12}. The precision in hydrogen on the same transition remains a few orders of magnitude higher [7]. Thus, the antihydrogen–hydrogen frequency comparison, whilst constituting a stringent CPT-invariance test, is dominated by the uncertainty of the result for antihydrogen. One of the major sources of uncertainty in the current best antihydrogen measurement is the accuracy of the frequency reference, which contributed 2 kHz to the overall uncertainty budget [6]. The laser frequency is stabilised to the resonance of an ultra-low expansion cavity, which is monitored via a femtosecond frequency comb referenced to the SI second via a GPS-disciplined quartz oscillator. Two thermal caesium atomic clocks are concurrently counted for further monitoring. To significantly reduce this source of uncertainty, ALPHA has upgraded the metrology suite to include an active hydrogen maser and a caesium atomic fountain frequency standard. Caesium fountains serve as primary standards, measuring the ground-state hyperfine transition frequency of caesium, and thereby leading to a realisation of the SI definition of the second [8]. Atomic fountains determine the hyperfine caesium transition frequency using Ramsey spectroscopy [9] of a laser cooled and trapped cloud of ultracold caesium atoms [10, 11]. These methods allow fountains to achieve fractional accuracies reaching 1.1×10^{-16} [12–16]. They provide international timekeeping, with primary standards contributing the majority of the measurements for the weighted mean that steers International Atomic Time (TAI).

Here, we report on the first evaluation of a caesium fountain primary standard located at CERN and operated within the ALPHA experiment, ALPHA-CsF1. The apparatus serves as an absolute frequency reference for antihydrogen spectroscopy. Although mobile primary standards have previously been deployed for precision laser spectroscopy [7], to our knowledge this is the first caesium fountain deployed permanently to serve as a direct local reference outside of a national metrology institute.

The paper is organised as follows: In section 2 we provide a description of the physics package, optics and microwave generation for the fountain. In section 3 we describe the fountain operation cycle. In section 4 we evaluate the effects of various systematic biases and calculate corrections to the measured frequency. In section 5 we characterise the short-term performance of the fountain and determine the long-term stability through GNSS comparisons. The operational remit of our caesium fountain is beyond accurate time keeping and particular details of the instrument may become of interest when interpreting results from the most precise future antihydrogen experiments where the fountain serves as a reference. We therefore include a review of some central features and background on systematic effects even if the fundamentals of fountain clocks are already well known.

2. Apparatus description

2.1. Physics package

The Cs fountain system consists of a physics package, optical systems, control electronics and microwave synthesis modules. It was designed and assembled by the National Physical Laboratory (NPL), and is an enhanced version of a system previously described in [17]. Here, we describe each of the key subsystems in turn.

A diagram of the central elements in the physics package is displayed in figure 1. State preparation and detection of the Cs atoms are performed in the lower region of the apparatus, which contains instrumentation for a magneto-optical trap (MOT), optical molasses (OM), optical pumping, and state detection. The interrogation of atoms occurs inside microwave cavities during their ballistic trajectory inside a hollow copper flight-tube in the magnetically shielded upper section of the physics package.

Caesium vapour is loaded into the reservoir chamber by crushing an ampoule which contains 1 g of Cs while an additional reserve ampoule is left intact for future supply. The reservoir is separated from the main fountain chamber by a valve, which enables replacement of Cs ampoules without the need to vent the entire vacuum system. The reservoir is temperature controlled using a Peltier element connected to a water-cooling circuit.

The MOT and OM are formed by three orthogonal pairs of counter-propagating laser beams and a pair of 345-turn coils situated on the outside of the vacuum chamber above and below the intersection of the laser beams. The six cooling laser beams are delivered from the light-distribution module to the physics package by optical fibres, along with repumping light which is overlapped with one of the horizontal cooling beams. The two coils are operated in an anti-Helmholtz configuration, producing a spatially varying quadrupolar magnetic field with a zero field region that overlaps with the intersection of the laser beams. This configuration forms a MOT that cools and confines the Cs atoms. Turning the MOT coils off forms an OM which is used for further cooling and launching the atom cloud. The ambient magnetic field of the Earth is compensated for in the lower region of the physics package using three pairs of rectangular coils that are adjusted and optimised manually to compensate all three orthogonal field components.

Directly above the MOT, two coils are placed in a Helmholtz configuration, providing a bias field for optical pumping. Above the optical pumping are two vertically separated regions for independent fluorescence detection of atoms in states $|F=3\rangle$ and $|F=4\rangle$ respectively. Guiding coils between the detection region and the magnetically shielded

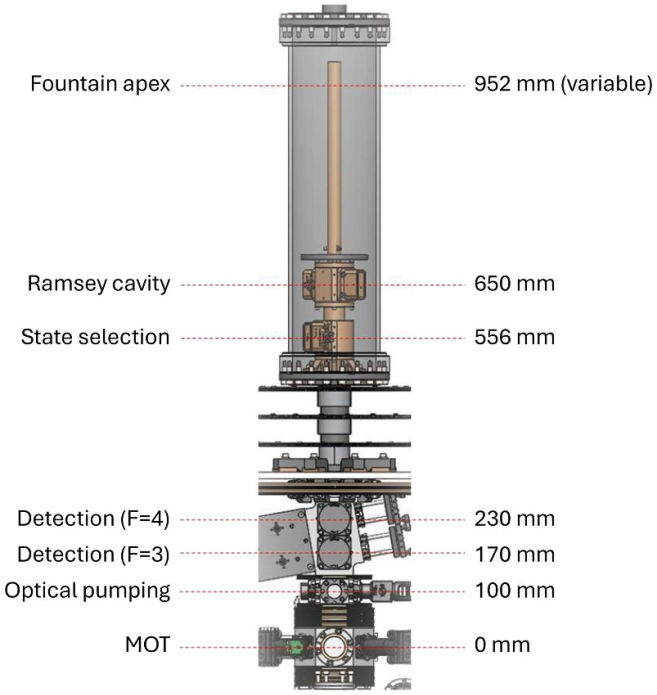

Figure 1. Overview of the physics package, with the Cs atom cloud height at the different stages indicated.

upper section eliminate magnetic field zeros and prevent accompanying Majorana spin mixing between Zeeman sublevels during atomic flight. All coils, except the lower MOT coil and compensation coils, therefore produce on-axis magnetic fields in the same direction.

There are two microwave cavities in the upper section of the physics package, referred to as the state selection and Ramsey cavity respectively (figure 1). Both microwave cavities are cylindrically symmetric with openings in the endcaps for the atoms to pass through, with dimensions tuned such that the TE_{011} mode is resonant with the clock transition. The state selection cavity transfers the atomic population from the $|F = 4, m_F = 0\rangle$ state to the $|F = 3, m_F = 0\rangle$ clock state. Population in the other m_F states can then be removed by a pulse of laser light resonant with the $F = 4$ state, leaving a pure sample of atoms in one clock state ready for interrogation in the Ramsey cavity. The state selection cavity is fed by a single rectangular cavity (TE_{012}), which couples to the main cylindrical cavity via a 1.5 mm radius circular hole in the cavity wall. The Ramsey cavity is used to interrogate the clock transition via the method of separated oscillating fields [9], providing a near $\pi/2$ microwave pulse each time the atoms pass through. The Ramsey cavity has been carefully designed to minimise the cavity distributed phase (DCP) [18] and is therefore symmetrically fed by two rectangular cavities, which couple to the Ramsey cavity via two 1 mm radius holes placed symmetrically about the midplane in the cavity wall. The TE_{011} mode of the Ramsey cavity has a quality factor of approximately 18 000 and is resonant with the Cs ground state hyperfine transition when the cavity is at 20 °C. The two cavities are situated within the double-walled aluminium flight tube. The temperature of the cavities is stabilised through the circulation of cooling water in the space between the walls, referred to as the water-cooling jacket, using a ThermoCube recirculating chiller. A narrow copper tube mounted on top of the Ramsey cavity acts as a waveguide below the cut-off frequency and protects the atoms from the effects of stray microwaves. Around the flight tube on the outside of the vacuum chamber, a coil produces a 114 nT vertical magnetic field, referred to as the C-field, which provides the quantisation axis and breaks the degeneracy of the m_F magnetic sub-levels–shifting the non-zero m_F states far off-resonance for state selection. The microwave cavities, flight tube, and coil are enclosed in three cylindrical layers of mu-metal magnetic shielding which provide an attenuation factor of over 10 000.

Ultra-high vacuum conditions are maintained in the system by a combination of ion getter pumps and non-evaporable getter pumps attached to the MOT chamber and the top of the flight tube chamber. In addition, shaped graphite getter materials are added in the region between the MOT and microwave cavities to reduce the amount of Cs background gas in the detection region. The entire vacuum system is baked for 8 weeks prior to first fountain operation, after which a residual background gas pressure of 2×10^{-11} mbar is reached.

2.2. Optical system

The optical setup for laser cooling, optical pumping and detection is schematically depicted in figure 2. The setup consists of three rack-mounted breadboards interconnected via fibres. A distributed Bragg reflector laser (DBR, Vescent D2-100-DBR-852-HP) provides light at the 852 nm D_2-line of ^{133}Cs with a typical linewidth of 250 kHz for addressing the $F = 4 \rightarrow F' = 5$ transition, shown together with all other relevant transitions (on resonance) in the energy level diagram in figure 3. The laser frequency is locked to the transition using Doppler-free saturated absorption spectroscopy (SAS) in a magnetically shielded Cs cell at room temperature on the spectroscopy board. A 4 MHz modulation of the laser current and differential detection of the two probe beams, one of which is overlapped with a pump beam in the backwards direction, yield an error signal for the locking servo acting on the laser current. A second slow feedback loop on the laser temperature is implemented to extend the locking range. Within the feedback loop, a double-pass acousto-optic modulator, referred to as the 'injection AOM', before the Cs cell on the spectroscopy board offsets the laser frequency from the $F = 4 \rightarrow F' = 5$ transition by an amount in the range 140 MHz–201 MHz to allow for various detunings during the fountain cycle as specified in section 3. The shifted frequency is sent to the fibre distribution board via a fibre-coupled tapered amplifier (TA, New Focus VAMP TA-7616) in a separate branch. The arriving 200 mW is split into eight different polarisation-maintaining (PM) fibres leading to the physics package. Six circularly polarised beams form the MOT. The four horizontal beams (labelled X_1, X_2, Y_1 and Y_2 in figure 2) are frequency shifted back to the cooling transition by a double-pass AOM with a fixed frequency of 201 MHz. The two vertical beams

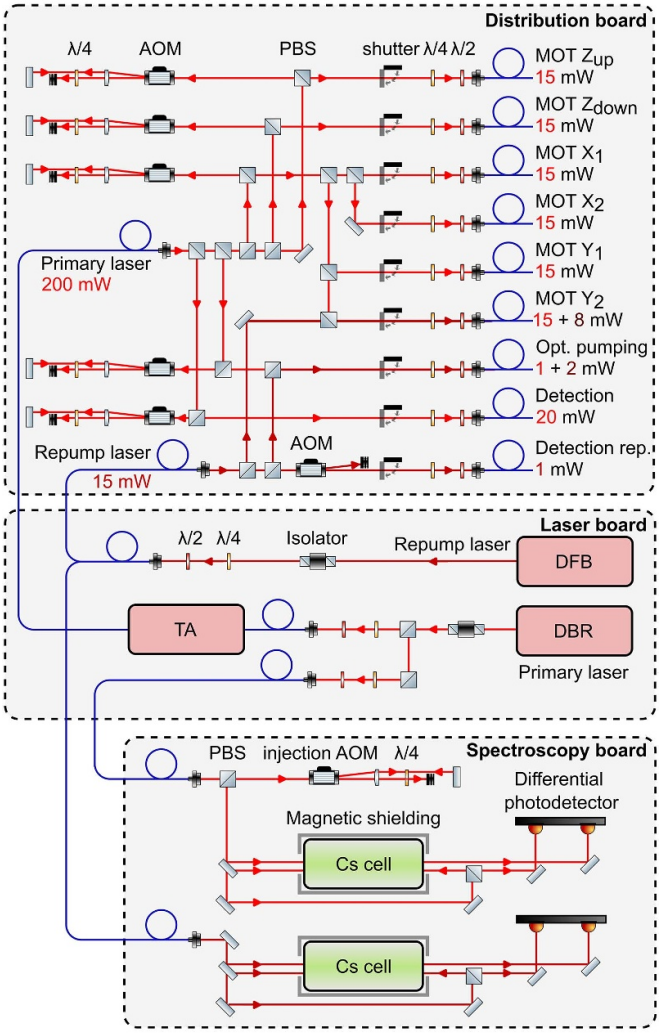

Figure 2. Overview of the optical system. AOM: acousto-optical modulator, PBS: polarising beampslitter, $\lambda/2, \lambda/4$: retardation plates, DBR: distributed Bragg reflector laser, DFB: distributed feedback laser, TA: tapered amplifier.

(labelled Z_{up} and Z_{down}) each have separate AOMs to form a moving molasses for launching the atom cloud by detuning the laser frequencies such that the counter-propagating beams have a frequency difference [19]. During the molasses and polarisation gradient cooling phase the frequency of all MOT beams is shifted further below resonance using the injection AOM. Light tuned 15 MHz above the $F = 4 \rightarrow F' = 4$ transition via a double-pass AOM at 377.8 MHz is delivered to the optical pumping region above the MOT, where an additional polarising beamsplitter (PBS) produces a pure π-polarisation aligned along the quantisation axis defined by the magnetic field of the Helmholtz coils. A retro-reflector on the other side of the vacuum chamber ensures symmetric photon scattering to avoid deflection of the atom cloud. The detection light is shifted to the $F = 4 \rightarrow F' = 5$ transition by an 160 MHz double-pass AOM.

A distributed feedback laser (DFB, Toptica DFB pro) with a linewidth of 3 MHz is tuned to the $F = 3 \rightarrow F' = 4$ transition and acts as a repumper to avoid accumulation of atoms in

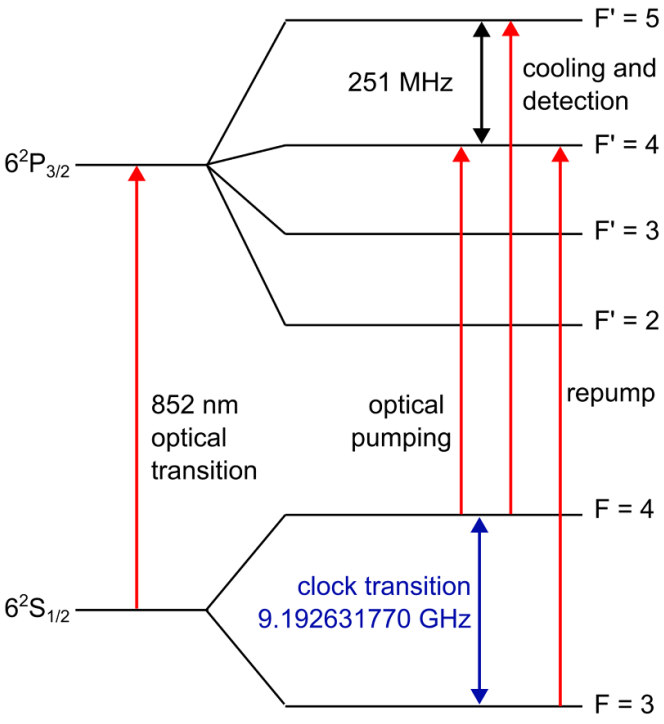

Figure 3. Hyperfine structure of the D_2 line of Cs.

the $F = 3$ state. Since repumping occurs on resonance during fountain operation, the repumper frequency is locked to this transition directly via a second SAS setup and a 20 kHz modulation of the diode current. On the distribution board, repumper light is overlapped with one of the MOT beams and the optical pumping beam. A third portion is fed into a separate fibre for atom detection through the zeroth order of an AOM. In this way, the power of all beams can be controlled by adjusting the radio-frequency (RF) power fed to the AOMs. All beams are additionally equipped with mechanical shutters operated by a small electromagnet to ensure that, when the shutters are off, no photons can reach the atoms during Ramsey interrogation. Two retardation plates are placed in front of each fibre for optimal matching of the light polarisation with the fast axis of the PM fibres.

All fibres are mounted on assemblies attached to flanges on the vacuum chamber. The power of each beam is monitored with small pick-up photodiodes attached to the side of each assembly and logged at the beginning of each fountain cycle. For the MOT and optical pumping beams, the divergent light emerging from the fibres is collimated to roughly 2.5 cm diameter by an $f = 100$ mm lens before entering the vacuum through anti-reflection coated windows. For state detection, two nearly horizontal beams are formed by a set of cylindrical lenses and a beamsplitter. The beams are highly elliptical and act as sheets of light through which the atoms fall during descent. The optics are mounted on a small breadboard attached to the vacuum chamber for good mechanical stability, as is shown in figure 1. A 10° angle from the horizontal plane prevents a thermal Cs beam coming out of the MOT chamber from being resonant with the detection light due to the induced Doppler shift [17]. Repumper light is added to the

lower beam for pumping atoms in the $F=3$ state into $F=4$ (see section 3). A half-wave plate enables balancing the power of both detection beams, while a set of graphite masks, also acting as a getter inside the vacuum chamber, truncates the beams to 18 mm in the horizontal direction to reduce scattering. Fluorescent light is collected through two windows perpendicular to the detection beams and focused onto two low-dark count amplified photodiodes through a band-pass filter to reduce background.

The entire optical system displays exemplary pointing and frequency stability as well as robust locking, which has been demonstrated by continuous operation over several months without user intervention.

2.3. Microwaves

Microwaves for feeding the Ramsey cavity are generated by a CS-1 model synthesiser from SpectraDynamics Incorporated. The synthesiser is provided with a 5 MHz reference frequency from the active hydrogen maser ALPHA-HM1 (T4Science iMaser 3000). Inside the CS-1, two ultra-low noise quartz oscillators convert this frequency to a 100 MHz signal, which references a dielectric resonant oscillator (DRO) that outputs 9.2 GHz with an accuracy much better than 1 Hz. A 7.368 230 MHz signal of a tunable direct digital synthesiser (DDS) with 48-bit resolution is mixed with the DRO output to yield microwaves for driving the $F=3\rightarrow F=4$ clock transition at 9 192 631 770 Hz. In this way, the frequency of ALPHA-HM1 is compared to the Cs clock transition.

Microwaves for supplying the state selection cavity are generated in a separate, home-built frequency chain. A high-frequency voltage controlled oscillator (VCO), phase-locked to the 10 MHz reference provided by ALPHA-HM1, generates a 4th harmonic signal at 9.210 GHz. Subsequent mixing with a 17.36 823 MHz RF signal from a DDS results in a microwave signal at the clock frequency. An automated variable attenuator acting on the RF component selects the microwave power which is delivered to the selection cavity such that the fractions of atoms transferred to the $|F=3,m_F=0\rangle$ clock state can be precisely controlled.

To avoid systematic shifts due to microwave leakage (see section 4.4), both microwave sources are detuned from resonance during the detection phase by rapidly changing the DDS RF frequency by 1 MHz (Ramsey cavity) or 6 MHz (selection cavity). In addition, during this time the selection microwave power is reduced to zero.

3. Fountain cycle

An overview of the operational cycle of the atomic fountain is shown in figure 4. The cycle lasts a total of 1.6 s, and comprises the five following phases:

(i) **Capture and cooling.** The laser light which cools and traps the caesium sample in the MOT is circularly polarised and tuned below resonance by 16 MHz. After roughly $\sim 10^8$ Cs atoms are captured and cooled in the MOT during 553 ms, the quadrupolar magnetic field is rapidly switched off and the cooling beams are extinguished for a 5–10 ms dark period. The duration of the dark period is adjusted to control the size of the Cs sample and minimise the collisional shift as discussed in section 4.2. Following the dark period the cooling beams are restored for a further 40 ms to perform OM cooling before launch while gradually increasing the frequency detuning.

(ii) **Launch.** During the 0.4 ms launch, the horizontal beams are extinguished, and the vertical beams are frequency shifted by a further +2.54 MHz (upwards) and −2.54 MHz (downwards), forming a moving molasses [19] that launches the Cs sample upwards at 4.3 m s^{-1}. Immediately afterwards, the horizontal beams are restored for a 1.9 ms phase of final polarisation gradient cooling during which the detuning of all cooling beams is ramped rapidly by −47 MHz and the beam intensity is gradually ramped to zero. This typically results in atom temperatures of a few micro-Kelvin and the population distributed between the 9 Zeeman sub-levels of the $|F=4\rangle$ state.

(iii) **State preparation.** Approximately 20 ms following the launch, the atomic sample traverses a pulsed horizontal beam of linearly polarised optical pumping light which is resonant with the $|F=4\rangle\rightarrow|F=4'\rangle$ transition. The matrix elements favour transitions between Zeeman sub-levels towards $m_F=0$ and with $m_F=0\rightarrow m_F'=0$ forbidden, the atomic population accumulates in the $|F=4,m_F=0\rangle$ state after multiple cycles of absorption and spontaneous emission [20]. To avoid overheating the sample, the optical pumping power is chosen such that the $|F=4,m_F=0\rangle$ is populated at $\sim 70\,\%$ as a trade-off between the number of atoms and the temperature that increases with stronger optical pumping. The atoms then traverse the resonant state-selection cavity, which provides a π pulse that transfers the population in the $|F=4,m_F=0\rangle$ state to the $|F=3,m_F=0\rangle$ state. Any remaining atoms in the $|F=4\rangle$ state are removed with a resonant 0.5 ms pusher pulse from the downward optical beam which deflects unwanted atoms out of the cold sample.

(iv) **Ramsey spectroscopy.** The atoms pass through the Ramsey cavity twice: once on their ascent, and a second time on their descent—the atoms continue their ballistic trajectory in the flight tube and do not experience the microwave field during the intermediate 0.5 s free-flight period [9]. The power of the microwave cavity is tuned such that the total time spent by the atoms moving through the cavity equates to a $\pi/2$ pulse with each pass. The microwaves are tuned by the synthesiser and when in fringe-tracking mode the microwaves alternate each cycle between 0.5 Hz above and below the clock-transition resonance, corresponding to half the width of the central Ramsey fringe.

(v) **Detection.** Following the second pass through the Ramsey cavity the atoms continue their descent into the detection region. Here, the population of each ground state is determined by collecting fluorescence induced by the two nearly horizontal upper and lower detection beams. The upper detection beam induces $|F=4\rangle\rightarrow|F'=5\rangle$ transitions, producing a fluorescence signal proportional to the

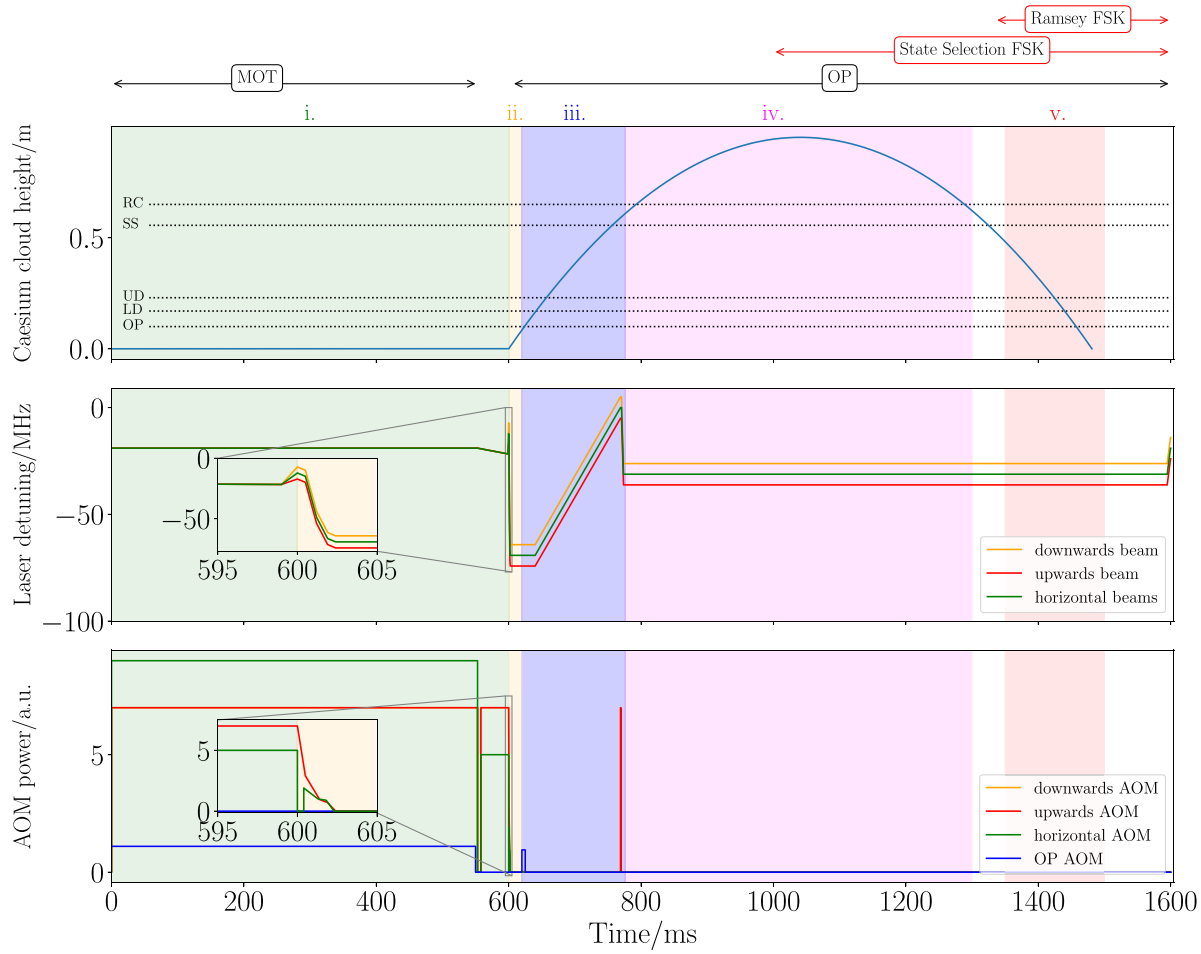

Figure 4. Overview of the Cs fountain cycle, showing the evolution of laser power, laser frequency and atom height during the cycle. The phases in Roman numerals are described in the main text. The insets display finer detail of the laser frequency detuning and power during the OM and launch phase, see main text for a full description. The black arrows indicate when current is applied to the MOT and OP coils, while the red arrows show when the selection and Ramsey cavity are frequency shifted from the Cs ground state hyperfine transition to reduce microwave leakage. The zero of the vertical axis in the top figure corresponds to the MOT position. OP: optical pumping, LD: lower detection region, UD: upper detection region, SS: state selection, RC: Ramsey cavity.

$|F=4\rangle$ population. The beam also accelerates the atoms, causing a shift off resonance when the atoms are passing through the lower detection beam. The lower detection beam contains light from both the primary and the repump lasers, and therefore the remaining population in $|F=3\rangle$ is rapidly pumped into $|F=4\rangle$, again producing a fluorescence signal. The normalised ratio

$$P = \frac{F_4}{F_4 + F_3}, \tag{1}$$

where F_3 and F_4 are the integrated and background-corrected fluorescence signals from the upper and lower detection regions respectively, provides a measurement of the clock-transition probability. With every two cycles, the difference $\delta\nu$ between the nominal frequency and the centre of the Ramsey fringe is calculated from the ratios measured with positive and negative detunings from the central fringe maxima using the relation

$$\delta\nu = \frac{m\,(P_+ - P_-)}{2}, \tag{2}$$

where m is the maximum slope of the central fringe, and P_+ and P_- are the ratios measured above and below the central fringe respectively. The nominal CS1 synthesiser frequency of the fringe centre is adjusted by $\delta\nu$ every second cycle, thereby tracking the frequency of the central fringe.

4. Systematic frequency corrections and uncertainties

The performance of the fountain is influenced by a number of systematic effects. Some of these effects introduce a shift in the measured clock frequency, a 'bias', which in most cases can be characterised by performing additional measurements. For other effects we provide an upper-limit estimate of the frequency deviation, which is then treated as an uncertainty in the final measurement result. In this section, relevant systematic effects are discussed, resulting in an estimate of the frequency uncertainty of the fountain.

4.1. Second order Zeeman shift

During the Ramsey interrogation, the clock transition is insensitive to magnetic shifts to first order. However, the second-order Zeeman effect, which produces the largest corrected frequency shift, must be quantified. From the Breit–Rabi formula [21] one can determine the fractional frequency shift induced by the second-order Zeeman effect on the clock transition [22, 23],

$$\frac{\delta\nu^{(2)}_{0\to0}}{\nu_0} = \frac{(g_J - g_I)^2\,\mu_B^2}{2h^2\nu_0^2}B^2. \tag{3}$$

Here, g_J and g_I are the electronic and nuclear gyromagnetic moments, μ_B is the Bohr magneton, B is the C-field, h is Planck's constant and ν_0 is the hyperfine splitting of the ground state. To map the C-field acting on the atoms during their flight in between passes through the Ramsey cavity, we measure the shift of the $|F=3,m_F=1\rangle \to |F=4,m_F=1\rangle$ transition, which is much more sensitive to C-field variations via the first-order Zeeman effect. The first-order Zeeman shift induced by the effect on the magnetically sensitive transition is also given by the Breit–Rabi formula

$$\frac{\delta\nu^{(1)}_{1\to1}}{\nu_0} = \frac{(g_J - g_I)\,\mu_B}{4h\nu_0}B. \tag{4}$$

Via equation (4), we can use the magnetically sensitive transition as a magnetometer by measuring $\delta\nu^{(1)}_{1\to1}$ with the Ramsey method. An additional complexity is that the second-order Zeeman shift of the clock transition is dependent on the time-averaged squared magnetic field, $\langle B^2\rangle$, that the atoms experience in their trajectory, whereas the magnetically sensitive transition is dependent on the time-averaged magnetic field, $\langle B\rangle$. The application of this technique therefore depends on the homogeneity of the field. In an inhomogeneous field

$$\langle B^2\rangle = \langle B\rangle^2 + \sigma_z^2, \tag{5}$$

where σ_z is the variance in the C-field experienced by the atom during its trajectory. To determine the homogeneity of the C-field, a map is constructed by launching the atoms to different heights above the Ramsey cavity and measuring $\delta\nu^{(1)}_{1\to1}$. An example map is displayed in figure 5, which demonstrates that the atoms experience a ∼114 nT magnetic field with a standard deviation below the 0.2 nT (<0.2%) level. This is sufficiently homogeneous that one can assume $\langle B^2\rangle = \langle B\rangle^2$ with a negligible error ($\sim10^{-18}$). Given that the C-field demonstrates sufficient uniformity, it is straightforward to combine equations (3) and (4) to obtain an expression for the frequency shift induced on the clock transition as a function of the measured shift on the magnetically sensitive transition

$$\frac{\langle\delta\nu^{(2)}_{0\to0}\rangle}{\nu_0} = 8\left(\frac{\langle\delta\nu^{(1)}_{1\to1}\rangle}{\nu_0}\right)^2. \tag{6}$$

The uncertainty of the second order Zeeman-shift correction originates from the long-term stability of the C-field. To estimate the uncertainty, the fractional frequency shift was measured at irregular intervals over 442 days for a range of launch heights with results shown in figure 6. The stability experienced by atoms launched to the full height of 95.05 cm is excellent over the entire period with a mean fractional shift, via equation (6), of 606.23×10^{-16}. We periodically re-evaluate the frequency correction based on the most recent C-field map. As a very conservative estimate of the corresponding uncertainty, we take from figure 6 the maximum observed C-field difference of 0.06 nT, resulting in an uncertainty of 0.6×10^{-16} on the clock frequency.

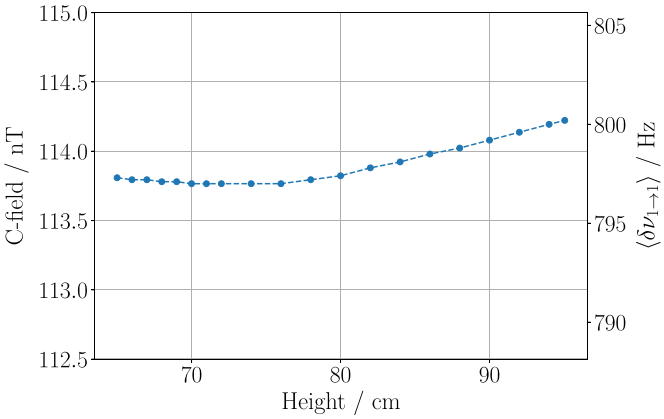

Figure 5. A map of the C-field measured by the technique described in the main text. The right axis displays the measured frequency shift $\delta\nu^{(1)}_{1\to1}$, whereas left axis displays the C-field which induces the shift. The zero of the horizontal axis refers to the MOT location as indicated in figure 1. The typical launch height is 95.05 cm.

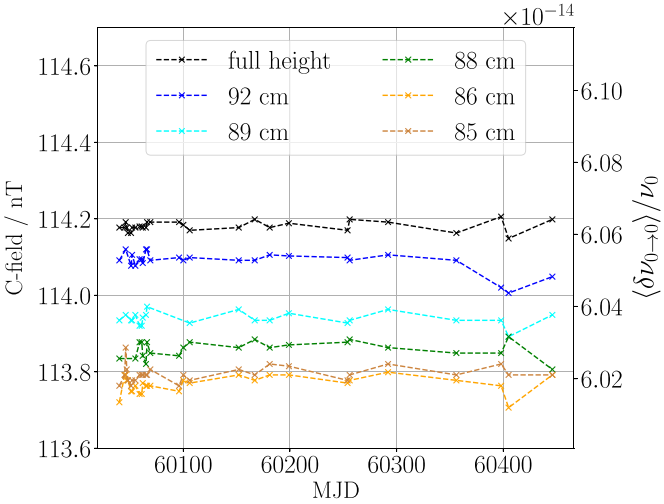

Figure 6. Drift of the C-field over time in Modified Julian Days (MJDs), and the corresponding fractional frequency shift of the clock transition. The full height (95.05 cm) is plotted in black, and lower heights plotted in different colours according to the legend. The axes are as in figure 5.

4.2. Collisional shift

The frequency shift caused by cold atom collisions is a major source of uncertainty in fountain standards [24]. The observed frequency shift emerges from perturbations in the energy

levels of the clock states due to collisions among atoms in the cloud in the ballistic flight during Ramsey interrogation. The size of this shift is proportional to the atom density and could therefore be reduced by operating the fountain at a low density. However, when operating with fewer atoms, the signal-to-noise (SNR) ratio and short-term stability of the fountain are also significantly reduced. Prior research has shown that the collisional rate coefficients for atoms in the two clock states in Cs are strongly dependent on the collision energy, and have the opposite sign for collision energies equivalent to 200 nK or less. Due to expansion of the atom cloud, impact energies in this regime are obtained in the fountain providing the cloud has an ensemble temperature of a few micro-Kelvin and an initial radius of the order of a millimetre [24]. It is therefore possible to cancel the collisional shift by making small adjustments to the state population after the first Ramsey pulse. Reaching the low collisional energy regime requires tuning the initial cloud size and atom temperature. For ALPHA-CsF1, an optimal initial cloud size is obtained by letting the atoms expand for 5 ms after the MOT-phase. All fountain parameters were then optimised to reach a temperature of 3.9 μK, measured from the width of the time-of-flight (ToF) detection signal. The fractional population in $F=4$ after the first Ramsey pulse can then be set to yield optimal cancellation of the collisional shift by adjusting the amplitude of the Ramsey pulses. The frequency shift can be estimated by alternating the operation of the fountain between low and high atom density as shown in figure 7, displaying a clear linear relationship between the shift size and $F=4$ population with a zero crossing at 0.48 ± 0.03. Operating the fountain at this optimum population fraction does not reduce the stability of the fountain. It is difficult to achieve full cancellation during long-term operation of the fountain, e.g. slight variations in temperature could lead to small variations in the microwave amplitude via shifting of the Ramsey cavity resonance frequency. Therefore, the residual shift is continuously measured by operating the fountain at two different densities and extrapolating the observed clock frequency to zero density [25]

$$\nu_{0,\mathrm{ext}} = \frac{k \cdot \nu_{\mathrm{LD}} - \nu_{\mathrm{HD}}}{k-1}, \tag{7}$$

where ν_{LD} and ν_{HD} are the measured frequencies at high and low density and k is the ratio between the two densities, which is measured by the number of detected atoms for each density $k \approx N_{\mathrm{HD}}/N_{\mathrm{LD}}$. The implicit assumption here is that there is a linear relationship between atom number and density, i.e. the cloud has the same spatial profile for both densities. Since we use the amplitude of the microwave field in the selection cavity to vary the atom density with $k \approx 7$, we do not have access to the cloud shape before it enters the Ramsey cavity. To estimate the size of the effect, we compare the ToF signals for both densities after the ballistic flight. This is shown in figure 8 where the residuals below 2% indicate close to identical cloud shapes for both densities. However, the detected ToF signals do not necessarily represent the initial spatial profile and the density ratio might be subject to a larger error, originating from spatial variations of the microwave field amplitude in the selection cavity. Detailed measurements performed in another Cs

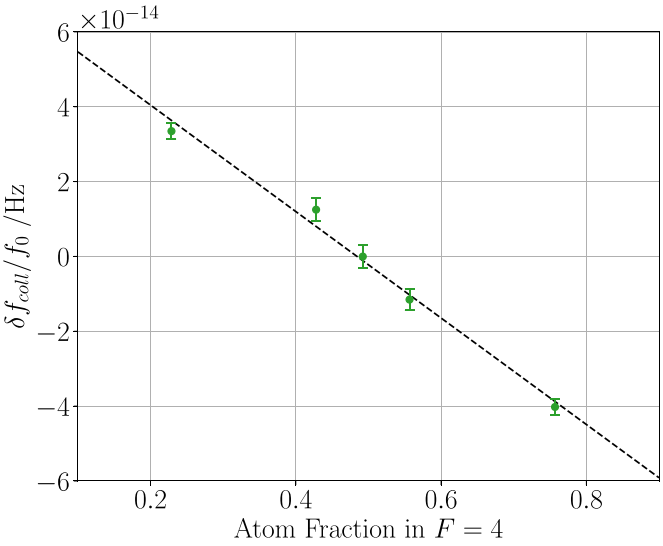

Figure 7. Frequency difference between high density and low density operation of the fountain, for different atom fractions in the $|F=4\rangle$ state after the first passage through the Ramsey cavity.

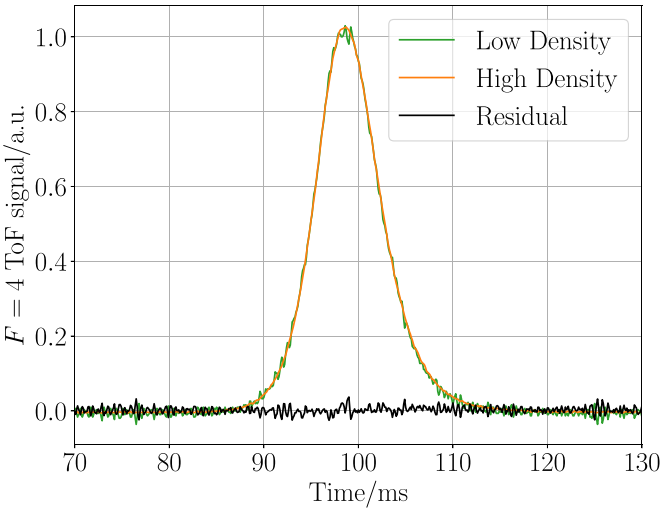

Figure 8. Time of flight (ToF) signal of the $|F=4\rangle$ atoms for high and low density operation.

fountain of the NPL design have indicated a fractional error in k of about 1% for a wide range of operating parameters [26]. Here, we conservatively assume a fractional error in k of 10%. The contribution of this effect to the type-B uncertainty in the extrapolated frequency is given by [27]

$$\sigma_{\mathrm{ext}} = \frac{\sigma_k}{(k-1)^2} \Delta F'_{H-L}, \tag{8}$$

where σ_k is the uncertainty in k and $\Delta F'_{\mathrm{H-L}} = \nu_{\mathrm{LD}} - \nu_{\mathrm{HD}}$ the measured collisional shift enlarged by its statistical uncertainty. Using $\sigma_k = 0.7$ and $\Delta F'_{\mathrm{H-L}} = 60 \times 10^{-16}$ as a typical value for the collisional shift during normal operation, we obtain a nominal systematic uncertainty of 1×10^{-16}. The uncertainty is re-evaluated frequently as part of the data analysis in operation as a frequency reference for the ALPHA experiment.

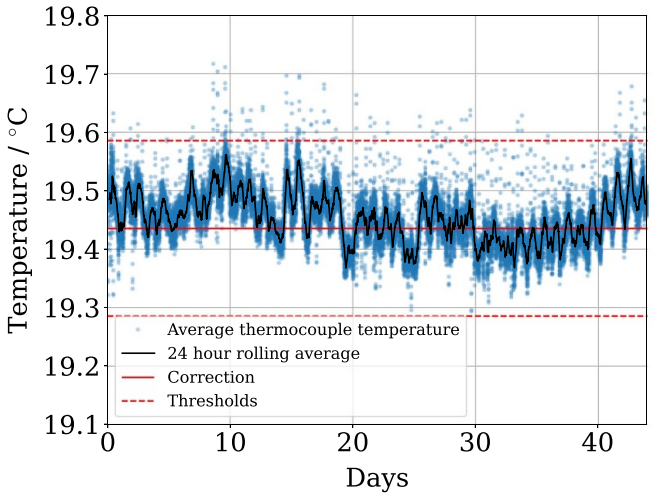

Figure 9. Temperature variation of the fountain flight tube water-cooling jacket as measured by three thermocouples mounted along the drift tube. The blue data points show how the average of the three thermocouples fluctuates over time, sampled at an interval of 2 min. The black curve displays a 24 h rolling average of the data.

4.3. Blackbody radiation (BBR) shift

Thermal radiation from the flight tube induces shifts in transition frequencies of the caesium atoms via the AC Stark and Zeeman effects. Assuming that the atoms can be approximated as being surrounded by a blackbody radiator at temperature T during the Ramsey interaction, the resulting fractional frequency shift has been determined [23, 28] to be given by

$$\frac{\Delta\nu_{\mathrm{BBR}}}{\nu_0} = \beta\left(\frac{T}{300\ \mathrm{K}}\right)^4\left[1+\varepsilon\left(\frac{T}{300\ \mathrm{K}}\right)^2\right], \qquad (9)$$

where the coefficients are $\beta = (-171.8 \pm 0.3) \times 10^{-16}$ and $\varepsilon = 0.013 \pm 0.001$ [29, 30]. To determine T we take an average of the temperatures read by three T-type thermocouples positioned along the length of the water-cooling jacket. The thermocouples were calibrated to an uncertainty of 0.1 K and all three thermocouples typically agree within the calibration uncertainty, which indicates that there are no significant temperature gradients in the flight tube. The resulting estimate of the uncertainty in T is ± 0.2 K, producing a fractional uncertainty in the black body radiation shift of $\mp 0.43 \times 10^{-16}$. The thermocouples monitor the temperature continuously, as displayed in figure 9. The fractional frequency shift induced by BBR and determined from the unweighted mean of all data in the period in figure 9 is $(-157.36 \pm 0.53) \times 10^{-16}$, which includes the combined uncertainties in β and ε. The correction for the blackbody shift is updated whenever the temperature averaged over 24 hours changes by more than 0.15 K from the temperature used for the previous correction, with the limits displayed by the dashed red lines in figure 9.

4.4. Microwave leakage

Despite a careful design to minimise the leakage of radiation from the microwave cavities, radiation exposure of the atoms when they are outside the Ramsey cavity cannot completely be avoided. Such interactions do not have an effect on the frequency measurement if they happen before the pusher pulse, which removes the population from $|F = 4, m_F = 0\rangle$ during the atom ascent in between the two microwave cavities. The copper tube above the Ramsey cavity and similar tubes between and below the microwave cavities extending down to the bottom of the magnetic shielding act as a waveguide and therefore strongly attenuate microwave radiation below the cut-off frequency, chosen well above the clock frequency by adjusting the diameter of the tube [14]. At apogee for a typical launch the centre of the cloud is about 100 mm from the end of the tube which leads to an attenuation of 60 dB. To minimise the effect of microwaves on the atoms after they exit the copper tubes, the microwave frequency is rapidly tuned off resonance after the second passage through the Ramsey cavity, using a frequency shift key (FSK) protocol on the microwave synthesiser. A similar procedure is applied to the state selection microwave synthesiser. The effect of residual microwave leakage on the transition probability is predicted to follow a sinusoidal behaviour as a function of microwave amplitude [31] and can be expressed as

$$\Delta P = c_{\mathrm{L}} A_{\mathrm{R}} \sin(A_{\mathrm{R}}) \sin(\omega_{\mathrm{mod}} T_{\mathrm{R}}), \qquad (10)$$

where c_{L} is a scaling factor that depends on the strength of the leakage field, A_{R} is the Rabi pulse area of the interaction of the atoms with the first pulse of microwaves on their ascent, $\omega_{\mathrm{mod}} = 2\pi f_{\mathrm{mod}} = \pi$ is the angular modulation frequency at which the atoms are interrogated, and T_{R} is the Ramsey interaction time between the two passages through the cavity. To characterise the effect of microwave leakage on the frequency of the fountain, a series of measurements was carried out with varying microwave amplitudes and toggling between detuned and resonant microwaves during the atom descent. To increase the sensitivity of this measurement, we have temporarily installed a microwave horn that irradiates the lower part of the fountain with the same microwave frequency that is fed to the Ramsey cavity [16]. The transition probability is obtained from the measured fractional frequency error $\Delta\nu$ and the fringe contrast C (defined as the difference in the observed ratio between a Ramsey measurement at the clock frequency and one detuned by 1 Hz) via $\Delta P = (\delta\nu/\nu_0)C\pi/2$. The result of one such measurement is shown in figure 10. Without FSK, a large transition probability shift is visible, following the trend from equation (10). When FSK is engaged, the frequency shift is much smaller, and depends on the exact timing of when the FSK is engaged. Tight FSK refers to the microwave detuning being applied straight after the cloud passes the Ramsey cavity for the second time, whereas for relaxed FSK the detuning occurs 10 ms later. For the data presented in section 5, relaxed FSK timing was used, whereas for future data the timing of the FSK was optimised to more tightly follow the second Ramsey cavity passage, resulting in a smaller frequency shift, as shown by the green points in figure 10(b). This measurement was repeated using a different location of the microwave horn, yielding similar results. As a conservative estimate of the

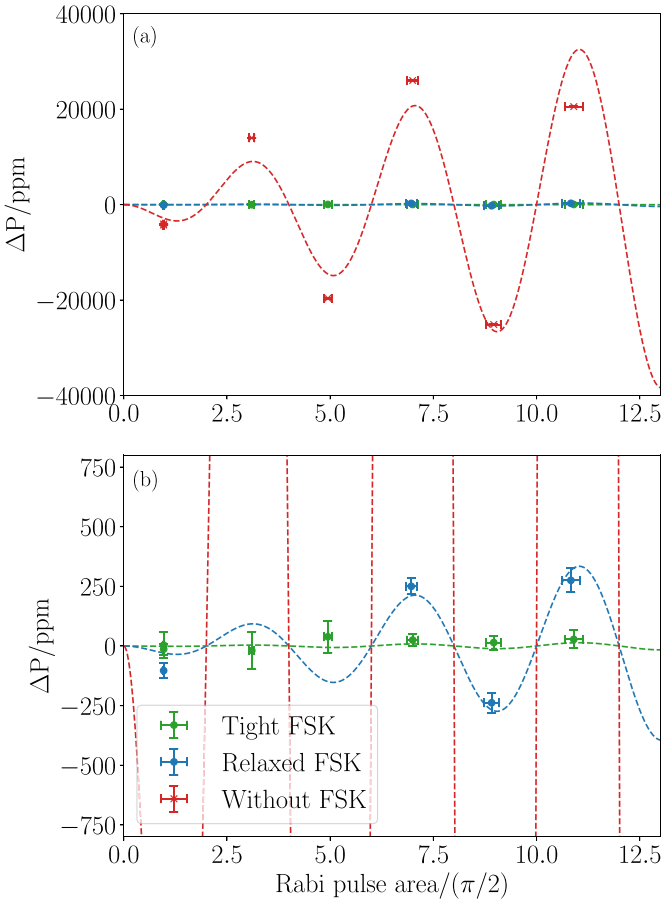

Figure 10. Systematic shift of the transition probability induced by microwave leakage from a microwave horn close to the MOT chamber as a function of A_R of the atoms on their ascent, which is varied by changing the microwave field amplitude fed to the Ramsey cavity. The horn is fed with microwaves from the same source as the Ramsey cavity. Three measurement series are presented in full scale (a) and zoomed-in vertically (b): tight FSK (green), relaxed FSK (blue) and resonant microwaves (no FSK, red).

reduction in the leakage-induced shift of the transition probability by the FSK protocol, we take the smallest observed ratios from the fitted models and obtain 68 and 255 for the relaxed and tight FSK timing, respectively. To assess the size of the microwave leakage shift during normal operation, we have performed multiple measurements of the same nature but without the presence of the microwave horn, during the period between September 2022 and December 2024. During this time we observed varying sizes of the leakage-induced shift when the FSK was not engaged. The origin of these fluctuations is unclear, and we note that small mechanical or temperature-induced changes in the physics package over time could lead to changes in the leakage microwave field. As a conservative upper bound on the size of the frequency shift during normal operation, we take the largest observed change during the entire period in the transition probability without FSK at a nominal Rabi pulse area of $\pi/2$, and divide it by the attenuation of the FSK protocol. This gives a small bias and results in an uncertainty of 1×10^{-16} for the relaxed FSK timing, and 3×10^{-17} for the tight FSK timing, since we do not correct for the bias.

4.5. AC Stark shift

During the Ramsey interrogation time, any stray electromagnetic radiation interacting with the atom cloud will induce an energy level shift of the clock states, altering the measured frequency. Therefore, care has to be taken to ensure that all laser beams are extinguished during this part of the clock cycle, especially the vertical beams which are passing through the flight tube region and are in view of the atoms at all times. Since all of the primary laser beams pass through AOMs, their power can be turned off and their frequency detuned to strongly attenuate the amount of light sent towards the fibres by at least 30 dB. Additionally, each of the laser paths has a mechanical shutter before light enters the optical fibre towards the physics package. To measure the effect of any residual AC-Stark shift from stray light, passing both the AOM and shutters, we operate the fountain while leaving the AOMs on during the clock measurement. In this way, we collected a data set where the AOMs were toggled on and off during atom interrogation between consecutive fountain cycles. From the measured frequency shift of $(-2.5 \pm 0.9) \times 10^{15}$, we infer a residual AC-Stark shift $< 10^{-17}$. The repumper beams for optical pumping and detection are not controlled with AOMs. To measure their influence on the clock transition, we toggled between normal fountain cycles and ones where the repumper shutters were left open. The measured frequency shift was $(-16.4 \pm 1.4) \times 10^{-15}$, and with -30 dB as a conservative estimate of the shutter attenuation, we infer the repumper AC-Stark shift to be $< 2 \times 10^{-17}$.

4.6. Gravitational red shift

ALPHA-CsF1 acts as a primary frequency standard at the location of operation. There is a difference in orthometric height between the free-flight region of the Cs atoms and the magnetic trap where antihydrogen spectroscopy experiments occur. For the fountain to be effective as an accurate reference for antihydrogen spectroscopy, the difference of gravitational redshifts must be determined. The relative gravitational redshift is given by [32]

$$\frac{\Delta\nu_g}{\nu_0} = \frac{W_{\bar{\mathrm{H}}} - W_{\mathrm{Cs}}}{c^2} = \frac{1}{c^2}\int_{H_{\mathrm{Cs}}}^{H_{\bar{\mathrm{H}}}} \boldsymbol{g}\cdot \mathrm{d}\boldsymbol{H}, \tag{11}$$

where $W_{\bar{\mathrm{H}}}$ and W_{Cs} are the gravitational potentials experienced by the antihydrogen and Cs atoms respectively, $\boldsymbol{H}$ is the orthometric height from the geoid, $H_{\bar{\mathrm{H}}}$ and H_{Cs} are the orthometric heights of the antihydrogen trap and the Cs fountain respectively, c is the speed of light and $\boldsymbol{g}$ is the local acceleration due to gravity. For small changes in height, the Earth's gravitational field is approximately uniform and

$$\frac{\Delta\nu_g}{\nu_0} = \frac{g}{c^2}\left(H_{\bar{\mathrm{H}}} - H_{\mathrm{Cs}}\right). \tag{12}$$

The orthometric heights were determined using the CERN Geographic Information System as 435.75 m and 443.61 m respectively relative to the EGM2008 geoid [33]. The Cs fountain height is taken as an average along the ballistic flight. Using equation (12), along with the local gravitational acceleration, $g = (980\,577\,858 \pm 4)\,\mu$Gal, measured at CERN by the Swiss Federal Office of Topography [34], produces a fractional redshift of $(-8.58 \pm 0.15) \times 10^{-16}$, where an uncertainty of 0.1 m has been applied to each orthometric height. The gravitational redshift is larger when the performance of ALPHA-CsF1 is evaluated against primary frequency standards operating in other locations, or against TT whose frequency is based on realisations of the SI second at the conventionally adopted equipotential of Earth's gravity (see section 5).

4.7. Microwave generation

Spurious spectral components in the frequency spectrum of the microwave source are a potential source of systematic frequency shifts, especially if they are within the Rabi excitation bandwidth, which for this system is on the order of a few tens of Hz. However, sidebands that are detuned symmetrically around the clock frequency do not have an effect [35]. To put an upper limit on this effect, we have measured the output spectrum of the CS-1 microwave synthesiser and found that although spurious signals of order –40 dBc were present, they were all arranged symmetrically around the main peak with asymmetries smaller than 0.5 dBc. We therefore estimate the possible effect on the clock frequency to be smaller than 1×10^{-16}.

4.8. Cavity pulling

The effect of radiative damping of the microwave field inside the Ramsey cavity by the atom cloud can shift the clock transition frequency. Since we operate at low atom numbers and also extrapolate to zero density by running the fountain at two different densities, this effect is negligibly small. Second order cavity pulling arises when the Ramsey cavity is driven away from its resonance frequency. This can result in the atoms experiencing slightly different microwave amplitudes on either side of the central Ramsey fringe and therefore induces an effective frequency shift. By tuning and stabilising the flight tube temperature to within 0.2 K, as shown in figure 9, we keep the microwave cavity resonance within 30 kHz of the clock frequency. Since we operate the fountain using a Rabi pulse area that is within 10 % of $\pi/2$, the resulting shift can be calculated to be below 1×10^{-17} using equation (5.6.123) in [36].

4.9. Distributed cavity phase (DCP) shift

A spatial variation of the phase of the microwave field inside the Ramsey cavity can lead to a shift of the clock frequency via the Doppler effect, known as the DCP. In practice, effects from a spatially varying phase can arise if the cloud is not launched precisely along the direction of gravity, e.g. due to a small tilt of the fountain, such that the cloud does not retrace its ascending path through the cavity on descent. Additionally, the cloud increases in size over time, and will therefore be larger on descent.

To characterise the induced frequency shift, it is helpful to express the spatial variations in the microwave field of a cylindrically symmetric cavity as an azimuthal Fourier series [37]. Since the atom cloud stays close to the axis of the cavity, we only need to consider the lowest order terms which we label with the Fourier index m. The $m = 0$ term describes frequency shifts that depend on microwave power. The Ramsey cavity in ALPHA-CsF1 was optimised to produce small $m = 0$ DCP shifts [38] at microwave amplitudes up to $6\pi/2$ Ramsey pulse areas [12]. Allowing for potential $\pm 5\%$ endcap surface resistance inhomogeneities and a $\pm 5\%$ imbalance between the upper and lower set of cavity feeds results in an uncertainty of $\pm 0.4 \times 10^{-16}$ for normal operation corresponding to $\pi/2$ pulses.

The $m = 1$ term represents a linear phase gradient near the cavity axis, which can be caused by a residual asymmetry in the excitation from the two rectangular feeding cavities (see section 2.1). By carefully balancing the microwave amplitude and phase of both excitations, using the atoms as feedback, we have reduced such asymmetries. The residual $m = 1$ DCP shift is then proportional to the distance between the positions at which the cloud centre of mass (CoM) passes through the cavity plane on the way up and down. By tilting the fountain we can vary this cavity crossing separation. A two-week measurement campaign was conducted for both the axis perpendicular and the axis parallel to the cavity feeds. To reduce the effect of slow drifts of the maser frequency, the fountain tilt was alternated every 24 h and the linear drift of the maser frequency has been subtracted from each data series. The observed frequency shifts are shown in figure 11, where dead-time effects during the measurement of the opposite tilt are included in the error bars and the origin of the horizontal axis represents the initial fountain tilt on that axis. The resulting DCP $m = 1$ shift is $(0.8 \pm 0.5) \times 10^{-16}$ mrad^{-1} and $(0.0 \pm 0.6) \times 10^{-16}$ mrad^{-1}, for the perpendicular and parallel axes, respectively.

To characterise the $m = 1$ frequency shift, we model the spatial distribution of the atom cloud during a fountain cycle and calculate the distance between the cavity axis and the CoM of the atom cloud as a function of the fountain tilt angle [39]. We measure the ToF signal and the fringe contrast after a single Rabi pulse during the upward trajectory of the cloud while varying the fountain tilt and obtain good agreement with our model after adjusting the horizontal position of the MOT in the model by a few millimetres, which is a plausible offset since we have not optimised the MOT position in the fountain. The uncertainty arising from the model is estimated by varying the initial parameters and observing the resulting change in the cavity crossing separation. At the initial fountain tilt, the cavity crossing separation is (2.1 ± 0) mm [(-1.9 ± 1.1) mm] for the perpendicular [parallel] axis. The frequency shift for the initial tilt is $(3.4 \pm 2.8) \times 10^{-16}$ [$(-0.2 \pm 2.4) \times 10^{-16}$], giving a total $m = 1$ frequency uncertainty of 4.9×10^{-16}, since we do not correct for the shift. For the tilts explored in figure 11 the caviy crossing separation is (4.1 ± 0.1) mm [(3.9 ± 1.1) mm].

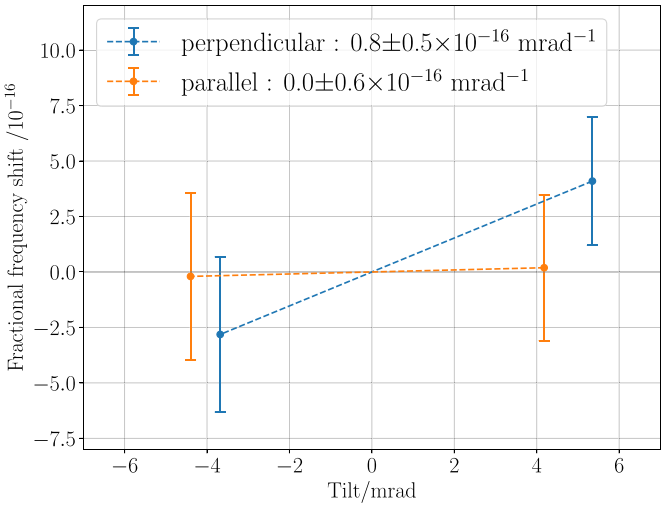

Figure 11. Frequency shift as a function of the tilt angle of the fountain for both the axes perpendicular and parallel to the cavity feeds. The indicated tilts are relative to the initial fountain tilt.

Based on this result, we were able to improve the tilt of the fountain in both axes to reduce the DCP $m=1$ contribution, such that for future measurements the frequency shift is $(0.7 \pm 1.8) \times 10^{-16}$ $[(-0.1 \pm 0.7) \times 10^{-16}]$, resulting in an $m=1$ frequency uncertainty of 2.0×10^{-16}.

The $m=2$ quadrupole variations of the cavity phase can lead to a frequency shift when combined with inhomogeneous detection along the feeding axis of the cavity, or with a displacement of the atom cloud from the central axis. We have evaluated the size of this shift for various MOT positions and launch angles based on the agreement between the model and the observed ToF signal and fringe contrast for the perpendicular and parallel directions separately. Here, we begin with the largest shift for initial MOT offsets and fountain tilts along the feed axis or those perpendicular to the feed axis. Our results suggest that the upward cavity traversal is azimuthally approximately $\pi/4$ from the feed axis, which would have a shift less than the maximum calculated. Conservatively considering the azimuthal upward position to be uncertain, we take the $m=2$ uncertainty to be the the largest shift divided by $\sqrt{2}$. This is 3.4×10^{-16} for the initial fountain tilt and 0.9×10^{-16} for the updated tilt. Future work that centres the MOT position on the fountain axis and accurately aligns the fountain vertically may significantly reduce the DCP uncertainties [39].

4.10. Microwave lensing

The Cs atoms traverse the microwave Ramsey cavity near the antinode of the standing wave field on the cavity's axis. The microwave field amplitude decreases quadratically away from the cavity axis [40], which imprints a phase shift on the atomic wavepackets that depends quadratically on the transverse position, acting as a lens. The lensing focuses and defocuses the dressed-state atomic wavepackets. This normally leads to the focused state being attenuated less by the cavity aperture, which produces an apparent frequency shift. The cavity design in ALPHA-CsF1 is based upon NPL-CsF3 where the DCP shift (section 4.9) is minimised [12], which may facilitate the observation of microwave lensing frequency shifts. Taking into account conservative uncertainties of the microwave amplitude, the MOT position and fountain tilt (0.23×10^{-16}), and neglected higher order lensing terms (0.2×10^{-16}) [13], we obtain a microwave lensing bias of $(0.84 \pm 0.30) \times 10^{-16}$, which we correct.

4.11. Phase transients

Phase variations of the microwave frequency that occur in between the two Ramsey interactions can lead to an observed frequency bias. Even tiny phase fluctuations on the order of microradians can lead to frequency shifts $\sim 10^{-16}$. If they occur randomly, they are averaged out over many fountain cycles, but when they occur synchronously, a shift can be induced. In our fountain, we use FSK to detune the microwave frequency after the second atom passage through the Ramsey cavity, which could potentially cause a phase shift synchronous with the fountain cycle. The FSK is switched on immediately after the second Ramsey interrogation, and switched off again at the start of the next cycle, around $\sim$750 ms before the first Ramsey pulse (see figure 4). Therefore, a possible phase transient from the switching of FSK will have decayed to negligible levels by the time of the first microwave interaction [41]. Another possible source of synchronous phase transients are background electromagnetic fields from the AOM amplifiers or laser beam shutters that are operated synchronously with the fountain cycle and could influence the CS-1 microwave synthesiser. However, none of these are operated during or in between Ramsey interrogations, mitigating the effect. Furthermore, we have placed the CS-1 synthesiser in a separate location that is several metres away from the AOM amplifiers and optical shutters to further suppress any interference. Together with reference data from a similar fountain design [14], we assess this effect to be $< 1 \times 10^{-16}$.

4.12. Second-order Doppler effect

Since the atom cloud is moving, the frequency of the clock transition is shifted with respect to the transition frequency of atoms in the laboratory frame by

$$\frac{\Delta\nu}{\nu_0} = -\frac{\langle v^2 \rangle}{2c^2}. \tag{13}$$

The launch height of 0.31 m above the Ramsey cavity leads to an average speed during the Ramsey interrogation of $\langle v^2 \rangle = 2\ \mathrm{m^2\ s^{-2}}$ [23] and a shift of 1×10^{-17}.

4.13. Magnetic field environment

The laboratory where ALPHA-CsF1 is installed is adjacent to the Antiproton Decelerator (AD) facility. To produce and collimate the antiproton beam, dipole and quadrupole magnets are ramped to a range of field strengths over the course of one production cycle, lasting about 110 to 130 seconds, after which the antimatter particles are delivered to experiments and the

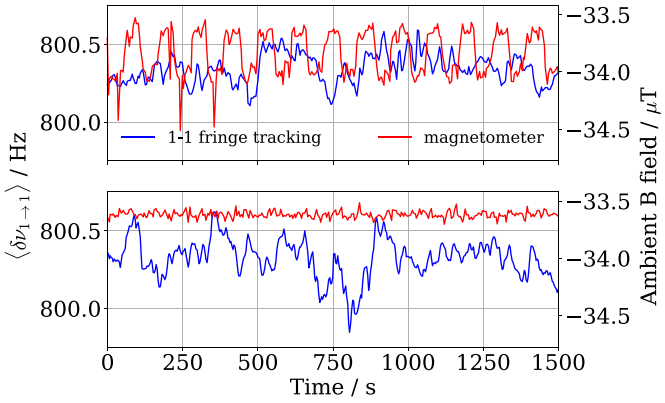

Figure 12. Plot of the magnetically sensitive transition frequency $\delta\nu^{(1)}_{1\to1}$ (left axis), compared to the ambient magnetic field measured by a magnetometer (right axis). The top plot displays behaviour of the fountain when the AD is cycling, whereas the bottom plot shows data without the AD cycling.

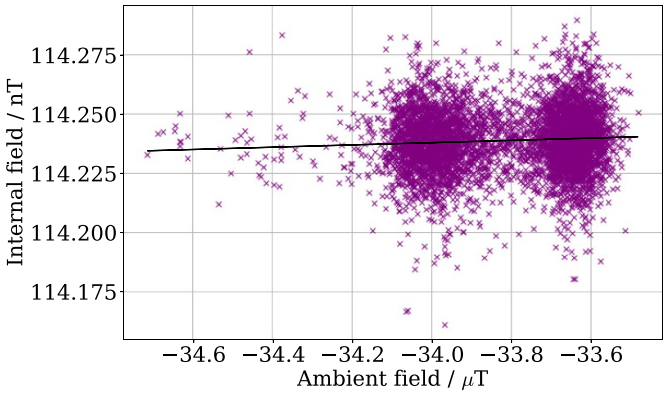

Figure 13. Plot of the external magnetic field parallel to the C-field versus the internal magnetic field measured by the magnetically sensitive transition frequency. Measurements were taken over approximately 12 hours. The black line displays the linear fit discussed in the main text.

process is repeated. As a consequence, the background magnetic field in the fountain laboratory oscillates with a period corresponding to the AD production cycle. The sensitivity of the clock transition to changes in the magnetic field is inherently small. In addition, any remaining effect should average to zero over time as the AD and fountain cycles are asynchronous. To study any remaining effect that the unique magnetic field environment of the AD might have on the clock performance, we have operated the fountain in a mode which tracks the central fringe of the $|F=3,m=1\rangle \to |F=4,m=1\rangle$ magnetically sensitive transition. These measurements can be compared to independent measurements of the ambient magnetic field parallel to the C-field, measured simultaneously by a magnetometer outside the magnetic shields. The results with and without AD magnet cycling are displayed in figure 12. As can be seen, when the AD is cycling the magnetometer measures a periodic variation in the ambient field, with an amplitude of around 500 nT.

The magnetically sensitive transition can be converted into a measurement of the C-field through equation (4). The internal field of the fountain can then be plotted against simultaneous measurements of the ambient magnetic field in the laboratory to look for correlations, as displayed in figure 13. There is very weak correlation to the linear fit of the data ($R = 0.07$), which has a slope of 4.8×10^{-6}. Taking the maximum recorded variation of 1.2 μT in the ambient magnetic field due to AD cycles corresponds to a variation of 6 pT in the field experienced by the Cs atoms, which produces negligible variation in the clock transition frequency through equation (3). From this we can conclude that the ambient magnetic field including effects from the AD has a negligible impact on the clock frequency.

4.14. Total systematic uncertainty

The contributions to the uncertainty budget as described in this section are summarised in table 1. The systematic uncertainties originating from microwave leakage and DCP have been reduced at the end of 2024 and the table presents values following this improvement. The long-term data presented in section 5 were taken before this improvement, and therefore have a higher systematic uncertainty of 6.4×10^{-16}. Currently, the total systematic uncertainty of the fountain is 3.0×10^{-16}.

Table 1. Uncertainty budget for the ALPHA-CsF1. All values are parts in 10^{-16}.

Effect	Bias	Uncertainty
Second order Zeeman[a]	606.23	0.6
Collisional shift[a]	60	1
BBR[a]	−157.36	0.53
Microwave leakage		0.3
AC Stark		0.2
Gravitational shift		0.15
Microwave lensing	0.84	0.30
Microwave generation		1
Cavity pulling		0.1
DCP $m=0$		0.4
DCP $m=1$		2
DCP $m=2$		0.9
Phase transients		1
Second order Doppler		0.1
Total	509.71	3.0

[a] Representative values for a typical fountain operation.

5. Performance evaluation

5.1. Statistical performance

To assess the short-term stability of the fountain, we define the SNR ratio as the inverse of the noise on the measured normalised ratio, with the atom fraction in $|F=4\rangle$ close to 0.5. The collisional shift cancellation enables fountain operation with relatively large atom numbers, resulting in excellent SNR characteristics, close to the shot-noise limit. To suppress the effects of frequency noise from the local oscillator

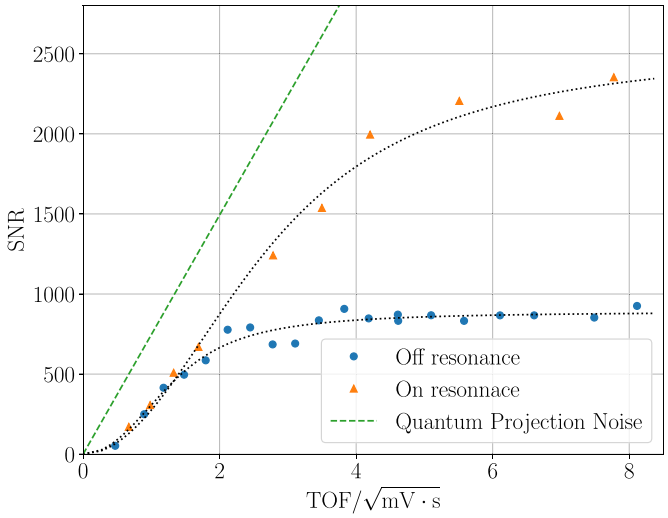

Figure 14. Signal to Noise (SNR) ratio as a function of the square root of the Time-of-Flight (ToF) signal, a measure of the number of detected atoms. Orange triangles were recorded on resonance, where the frequency noise from the local oscillator is suppressed, whereas the blue circles were measured off resonance where the SNR is limited by frequency noise. The dotted lines are fits to the data that include these three different noise contributions.

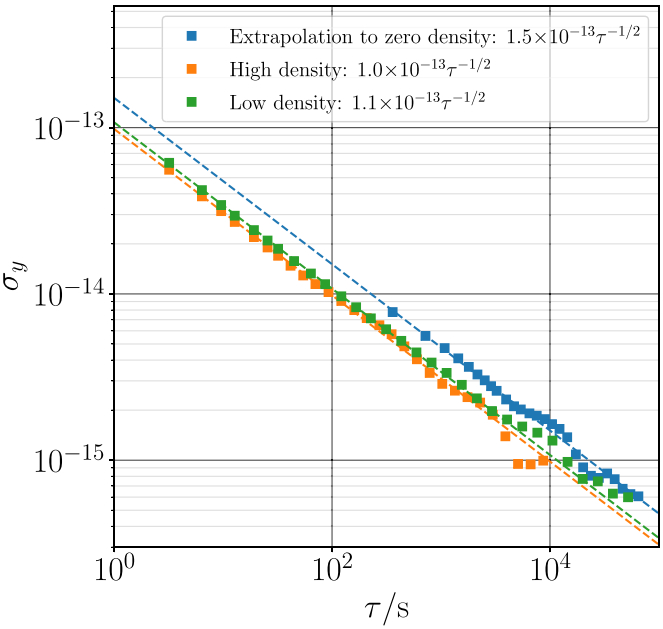

Figure 15. Short-term stability of the fountain for the measured frequency extrapolated to zero density (blue), high density operation (orange) and low density operation (green). The dashed lines represent $1/\sqrt{\tau}$ fits to the data.

on the SNR measurement, we apply resonant microwaves in a single Rabi pulse. The result is shown by the orange triangles in figure 14 as a function of the square root of the ToF signal, which is proportional to the atom number. The fitted model (dotted black line) encompasses three different noise sources. At low atom number, technical noise is dominating, e.g. from electronic noise in the detectors, appearing as a parabolic trend due to the square root of the horizontal axis. Quantum projection noise scales as $1/\sqrt{n_{\text{det}}}$ with n_{det} the number of detected atoms, and ideally the fountain follows this trend, shown by the green dashed line in figure 14. For large atom numbers, the component proportional to the fountain signal becomes leading, which could be due to laser amplitude or frequency fluctuations, effectively limiting the SNR to around 2300. This signal-to-noise level corresponds to a short-term stability limit of $4.7\times10^{-14}\tau^{-1/2}$. When operated in frequency measurement mode ('fringe tracking'), the measurement stability is limited by frequency noise from the local oscillator; the RF synthesiser in the maser, ALPHA-HM1. This is indicated by the blue circles in figure 14, which show a plateau at a SNR around 900. The short-term stability for high and low density are shown in figure 15 as overlapping Allan deviation curves. Both data sets closely follow a $\tau^{-1/2}$ behaviour, indicating white frequency noise as the dominant noise process. The small difference between the two densities indicates that the fountain is not limiting the stability even at low density. The behaviour of the frequency after extrapolation to zero density is also shown. The statistical performance of the fountain is in practice often limited by the low density signal. The fountain shows only a small drop in SNR even at less than 10 % of the maximum signal level, resulting in an excellent short-term frequency stability of $1.5\times10^{-13}\tau^{-1/2}$.

5.2. *Frequency comparisons*

To assess the long-term accuracy of the ALPHA-CsF1 fountain as an absolute frequency reference, we conduct a comparison with Terrestrial Time (TT) via a chain of linked time and frequency measurements. The comparison was performed from January 2023 to June 2024, with occasional interruptions due to systematic shift evaluations, equipment failures, power cuts, etc. The comparision was conducted with the initial tilt alignment (section 4.9). Firstly, with the fountain we record the frequency of the ALPHA-HM1 maser, which is located in the same laboratory, and apply periodic corrections to the ALPHA-HM1 frequency to minimise the frequency drift and offset. The ALPHA-HM1 frequency data produced by the fountain y(ALPHA-CsF1 − ALPHA-HM1) is binned in 1 h intervals, subtracting the total systematic bias that contains the specific second order Zeeman, collisional, and BBR shift evaluation for that bin, as outlined in table 1. The resulting dataset is segmented into intervals with a minimum of five days (the shortest period of continuous data) and a maximum of 39 d where the longest period of continuous data of 78 d was divided into two segments. The second part of the chain compares ALPHA-HM1 against a local timescale using common-view GNSS comparison via a satellite receiver (Septentrio PolaRx5) [42]. For the evaluation presented here we have compared against the UK timescale UTC(NPL) to obtain y_d(ALPHA-HM1 − UTC(NPL)). This comparison is binned in 24 h intervals and corrected for the gravitational shift due to the 443.61 m orthometric height of ALPHA-CsF1, which results in a fractional frequency difference of 4.840×10^{-14} compared to TT. The third part of the chain consists of the y_d(UTC(NPL) − UTC) time difference, which is

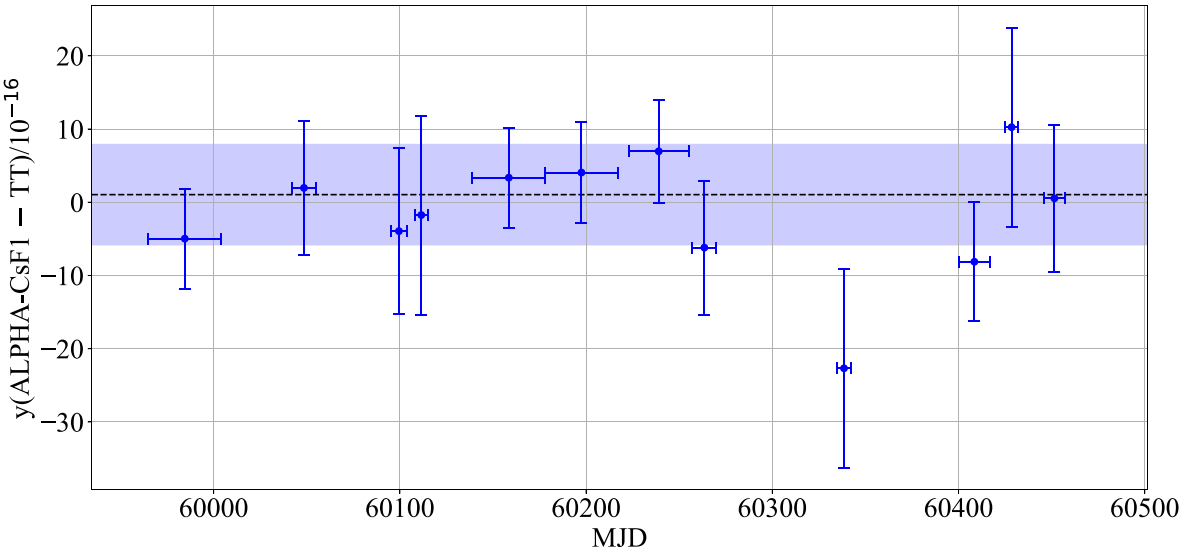

Figure 16. Fractional frequency difference between ALPHA-Cs1 and the SI second as realised by TT. The horizontal bars indicate the duration of a measurement period. Vertical bars represent the uncertainty of the GNSS link, combined in quadrature with the 6.5×10^{-16} systematic uncertainty for the measurement period. The average difference for the entire period, $(1.0 \pm 6.9) \times 10^{-16}$, is displayed by the horizontal dashed line, with the shaded region representing the total combined statistical and systematic uncertainty of the comparison.

accessible via the monthly published Circular T reports from the International Bureau of Weights and Measures (BIPM). We interpolate the five-day time differences provided in the reports with a third order polynomial to obtain daily values, which are converted into units of fractional frequency. Finally, to arrive at the SI second, we incorporate the d parameter, a correction to UTC/TAI that is published also in Circular T as a one-month average from all primary and secondary frequency standards contributing to TAI. We evaluate $y_d(\mathrm{UTC/TAI} - \mathrm{TT}) = -d$ by taking the d parameter as a fixed value during each one-month interval to obtain daily time offsets. The resulting frequency comparison $y_d(\mathrm{ALPHA\text{-}CsF1} - \mathrm{TT})$ is shown in figure 16, where the horizontal bars indicate the length of each of the datasets. The statistical uncertainties for the full frequency comparison chain are estimated from the Allan deviation curve of $y_d(\mathrm{ALPHA\text{-}CsF1} - \mathrm{TT})$ of the longest uninterrupted measurement period (78 d). The Allan deviation is fit with a τ^{-1} model, as the stability is dominated by phase noise from the GNSS Common View comparison. The vertical bars in the figure are then given by the model evaluated at a time corresponding to the length of each segment, combined in quadrature with the systematic uncertainty for the measurement period. The weighted average over the entire measurement period gives a fractional frequency difference of $(1.0 \pm 2.2(\mathrm{stat.}) \pm 6.5(\mathrm{syst.})) \times 10^{-16}$, with a reduced chi-square of $\chi^2 = 0.68$. The systematic uncertainty, which we assume does not decrease with averaging, is a combination of the ALPHA-CsF1 systematic uncertainty 6.4×10^{-16} (before the fountain tilt angle and microwave leakage timing were optimised), and the total uncertainty of the estimate of the d parameter listed in Circular T. The observed frequency difference is also well within the improved systematic uncertainty 3.0×10^{-16} of ALPHA-CsF1 after this measurement campaign finished.

6. Conclusion

We have evaluated the performance of the primary frequency standard, ALPHA-CsF1, for the ALPHA experiment at CERN and found that the fountain shows an excellent short-term stability. We have characterised the systematic frequency bias and we have optimised the operation of the fountain with reduced systematic uncertainty. We have carried out a frequency comparison between ALPHA-CsF1 and TT for approximately 500 days, and demonstrated agreement to within the uncertainties when the gravitational shift is taken into account. ALPHA-CsF1 provides the ALPHA experiment a local realisation of the SI second with a frequency uncertainty commensurate with the reference used in the most precise hydrogen spectroscopy [7] and more than three orders of magnitude improvement over the reference used for antihydrogen [6]. The improvement will facilitate more precise hydrogen–antihydrogen comparisons in future. ALPHA-CsF1 is to our knowledge the only primary frequency standard operated outside the scope of a national metrology institute. This creates numerous opportunities to contribute to precise timing and synchronisation in other experiments and facilities at CERN e.g. in the high-luminosity upgrade of the large Hadron collider. Finally, future frequency comparisons, including those via optical fibre networks [43], could enable ALPHA-CsF1 to contribute to the steering TAI as well as further pushing the limits of antimatter frequency measurements.

Acknowledgements

We acknowledge Peter Lovelock (NPL) for mechanical design support, and François Butin and Nicolas Roget (CERN) for help with organising the installation of the metrology laboratory. This work was supported by the EPSRC (UK), the

Carlsberg Foundation (Denmark), the European Research Council through its Grant programme (JSH) and the United States National Science Foundation under Award No. 2012117 (KG).

ORCID iDs

J Nauta 0000-0002-3477-7104
J Schoonwater 0000-0001-5152-4830
C Ø Rasmussen 0000-0002-6029-1730
N Madsen 0000-0002-7372-0784
K Gibble 0000-0003-3652-9638
K Szymaniec 0000-0002-3523-278X
S Eriksson 0000-0002-5390-1879

References

[1] Andresen G B *et al* 2010 Trapped antihydrogen *Nature* **468** 673
[2] Ahmadi M *et al* 2017 Observation of the hyperfine spectrum of antihydrogen *Nature* **548** 66
[3] Ahmadi M *et al* 2018 Observation of the 1S-2P Lyman-α transition in antihydrogen *Nature* **561** 1
[4] Ahmadi M *et al* 2017 Observation of the 1S-2S transition in trapped antihydrogen *Nature* **541** 506
[5] Baker C J *et al* 2025 Precision spectroscopy of the hyperfine components of the 1S–2S transition in antihydrogen *Nat. Phys.* **21** 1–7
[6] Ahmadi M *et al* 2018 Characterization of the 1S-2S transition in antihydrogen *Nature* **557** 71
[7] Parthey C G *et al* 2011 Improved measurement of the hydrogen $1S-2S$ transition frequency *Phys. Rev. Lett.* **107** 203001
[8] Barrell H 1969 Thirteenth general conference of weights and measures *Phys. Bull.* **20** 61
[9] Ramsey N F 1950 A molecular beam resonance method with separated oscillating fields *Phys. Rev.* **78** 695
[10] Chu S and Wieman C 1989 Laser cooling and trapping of atoms: introduction *J. Opt. Soc. Am. B* **6** 2020
[11] Wynands R and Weyers S 2005 Atomic fountain clocks *Metrologia* **42** S64
[12] Szymaniec K, Lea S N, Gibble K, Park S E, Liu K and Głowacki P 2016 NPL Cs fountain frequency standards and the quest for the ultimate accuracy *J. Phys.: Conf. Ser.* **723** 012003
[13] Weyers S, Gerginov V, Kazda M, Rahm J, Lipphardt B, Dobrev G and Gibble K 2018 Advances in the accuracy, stability and reliability of the PTB primary fountain clocks *Metrologia* **55** 789
[14] Beattie S, Jian B, Alcock J, Gertsvolf M, Hendricks R, Szymaniec K and Gibble K 2020 First accuracy evaluation of the NRC-FCs2 primary frequency standard *Metrologia* **57** 035010
[15] Gerginov V, Hoth G W, Heavner T P, Parker T E, Gibble K and Sherman J A 2025 Accuracy evaluation of primary frequency standard NIST-F4 *Metrologia* **62** 035002
[16] Beattie S, Jian B, Marceau C, Gibble K and Gertsvolf M 2025 Advancements in the NRC-FCs2 primary frequency standard *Metrologia* **62** 035003
[17] Hendricks R J, Ozimek F, Szymaniec K, Nagorny B, Dunst P, Nawrocki J, Beattie S, Jian B and Gibble K 2019 Cs fountain clocks for commercial realizations-an improved and robust design *IEEE Trans. Ultrason. Ferroelectr. Freq. Control* **66** 624
[18] Li R and Gibble K 2010 Evaluating and minimizing distributed cavity phase errors in atomic clocks *Metrologia* **47** 534
[19] Berthoud P, Fretel E and Thomann P 1999 Bright, slow and continuous beam of laser-cooled cesium atoms *Phys. Rev. A* **60** R4241
[20] Szymaniec K, Noh H-R, Park S and Takamizawa A 2013 Spin polarization in a freely evolving sample of cold atoms *Appl. Phys. B* **111** 527
[21] Breit G and Rabi II 1931 Measurement of nuclear spin *Phys. Rev.* **38** 2082
[22] Steck D 2024 Cesium D line data; (revision 2.3.3) (available at: https://steck.us/alkalidata/)
[23] Szymaniec K, Chałupczak W, Whibberley P B, Lea S N and Henderson D 2005 Evaluation of the primary frequency standard NPL-CsF1 *Metrologia* **42** 49
[24] Szymaniec K, Chałupczak W, Tiesinga E, Williams C J, Weyers S and Wynands R 2007 Cancellation of the collisional frequency shift in caesium fountain clocks *Conf. on Coherence and Quantum Optics* (Optica Publishing Group) (available at: https://opg.optica.org/abstract.cfm?URI = CQO-2007-CSuA13) p CSuA13
[25] Szymaniec K, Park S E, Marra G and Chałupczak W 2010 First accuracy evaluation of the NPL-CsF2 primary frequency standard *Metrologia* **47** 363
[26] Beattie S and Jian B 2023 Characterization of the collisional frequency shift in an atomic fountain clock using absorption imaging *Metrologia* **60** 045004
[27] Szymaniec K and Park S E 2011 Primary frequency standard NPL-CsF2: optimized operation near the collisional shift cancellation point *IEEE Trans. Instrum. Meas.* **60** 2475
[28] Itano W M, Lewis L L and Wineland D J 1982 Shift of $^2S_{\frac{1}{2}}$ hyperfine splittings due to blackbody radiation *Phys. Rev. A* **25** 1233
[29] Rosenbusch P, Zhang S and Clairon A 2007 Blackbody radiation shift in primary frequency standards *2007 IEEE Int. Frequency Control Symp. Joint With the 21st European Frequency and Time Forum* (https://doi.org/10.1109/FREQ.2007.4319241) p 1060
[30] Angstmann E J, Dzuba V A and Flambaum VV 2006 Frequency shift of hyperfine transitions due to blackbody radiation *Phys. Rev. A* **74** 023405
[31] Shirley J H, Levi F, Heavner T P, Calonico D, Dh Y and Jefferts S R 2006 Microwave leakage-induced frequency shifts in the primary frequency Standards NIST-F1 and IEN-CSF1 *IEEE Trans. Ultrason. Ferroelectr. Freq. Control* **53** 2376
[32] Pavlis N K and Weiss M A 2017 A re-evaluation of the relativistic redshift on frequency standards at NIST, Boulder, Colorado, USA *Metrologia* **54** 535
[33] Pavlis N K, Holmes S A, Kenyon S C and Factor J K 2012 The development and evaluation of the Earth Gravitational Model 2008 (EGM2008) *J. Geophys. Res.* **117** B4
[34] Topography of SFO National gravity network (available at: https://map.geo.admin.ch/?topic = swisstopo&zoom = 9&bgLayer = ch.swisstopo.pixelkarte-farbe&lang = en&layers = ch.bav.haltestellen-oev,ch.swisstopo.landesschwerenetz&E = 2493160.50&N = 1120934.80) (Accessed 22 April 2024)
[35] Levi F, Shirley J H, Heavner T P, Yu D-H and Jefferts S R 2006 Power dependence of the frequency bias caused by spurious components in the microwave spectrum in atomic fountains *IEEE Trans. Ultrason. Ferroelectr. Freq. Control* **53** 1584
[36] Audoin J V C 1989 *The Quantum Physics of Atomic Frequency Standards* (CRC Press)
[37] Guéna J, Li R, Gibble K, Bize S and Clairon A 2011 Evaluation of doppler shifts to improve the accuracy of primary atomic fountain clocks *Phys. Rev. Lett.* **106** 130801
[38] Gibble K, Lea S N and Szymaniec K 2012 A microwave cavity designed to minimize distributed cavity phase errors

in a primary cesium frequency standard *2012 Conf. on Precision Electromagnetic Measurements* p 70 (https://doi.org/10.1109/CPEM.2012.6251122)
[39] Burrows K, Hendricks R J, Szymaniec K, Gibble K, Beattie S and Jian B 2020 Measuring atom positions in a microwave cavity to evaluate distributed cavity phase shifts *Metrologia* **57** 065003
[40] Gibble K 2006 Difference between a Photon's Momentum and an Atom's Recoil *Phys. Rev. Lett.* **97** 073002
[41] Santarelli G *et al* 2009 Switching atomic fountain clock microwave interrogation signal and high-resolution phase measurements *IEEE Trans. Ultrason. Ferroelectr. Freq. Control* **56** 1319
[42] Allan D and Weiss M 1980 Accurate time and frequency transfer during common-view of a GPS satellite 334 (https://doi.org/10.1109/FREQ.1980.200424)
[43] Cantin E *et al* 2024 REFIMEVE frequency and time network and applications *J. Phys.: Conf. Ser.* **2889** 012031